
# High-temperature corrosion of weld overlay coating/bulk FeCrAl exposed in O2 + H2O + KCl(s) at 600 °C – A microstructural investigation

Available online at www.sciencedirect.com

jmr&t Journal of Materials Research and Technology

journal homepage: www.elsevier.com/locate/jmrt

# High-temperature corrosion of weld overlay coating/bulk FeCrAl exposed in $O_2 + H_2O + KCl(s)$ at 600 °C – A microstructural investigation

*Imran Hanif* [a,c,*], *Vicent Ssenteza* [a], *Johan Eklund* [a], *Johanna Nockert Olovsjö* [b], *Torbjörn Jonsson* [a]

[a] *Environmental Inorganic Chemistry, Department of Chemistry and Chemical Engineering, Chalmers University of Technology, SE-412 96, Göteborg, Sweden*

[b] *Kanthal AB, Hallstahammar, Sweden*

[c] *Energy Technology Center, RISE Research Institutes of Sweden*

ARTICLE INFO

*Article history:*
Received 6 May 2023
Accepted 8 July 2023
Available online 20 July 2023

*Keywords:*
FeCrAl
Weld overlay coating
High-temperature corrosion
Dilution
TEM
STEM-EDX

ABSTRACT

This work investigates the impact of high-temperature corrosion behavior of the newly developed FeCrAl alloy Kanthal® EF101 bulk material and weld overlay coating in the presence of KCl(g)/KCl(s) at 600 °C. The oxide scale formed within the secondary corrosion regime after exposure and the impact of alloy microstructure on corrosion behavior was investigated using scanning transmission electron microscopy. The findings indicated the key microstructural differences is the alloy grain size which influences the formation of a protective scale. In addition, It is indicated that coating exhibited inferior performance than the bulk material, primarily attributed to the microstructural differences.



## 1. Introduction

In recent years, there has been an increased global awareness of the necessity to reduce carbon dioxide ($CO_2$) emissions and transition from fossil fuels to alternative energy sources. Many countries across the world have set targets to systematically reduce the emission of greenhouse gases by more than 45–55% by 2030 compared to 1990 [1,2]. The shift from using conventional fuels to utilizing fuels such as biomass and waste in powerplants is one example of how to obtain carbon neutral energy. However, the combustion of biomass and waste produces high amounts of corrosive species, which causes rapid degradation of metallic components at the fireside of the boilers, especially the superheater tubes which results into reduced material life-time, high maintenance costs and reduced electrical efficiency of these plants [3,4].

Low-alloyed steels may be used as superheater materials at lower temperatures in power plants due to their good mechanical properties and low prices, however these materials suffer severe corrosion challenges in these harsh environments [5,6]. On the other hand, stainless steels may be used in areas with higher temperatures or more severe corrosion

* Corresponding author. Environmental Inorganic Chemistry, Department of Chemistry and Chemical Engineering, Chalmers University of Technology, SE-412 96, Göteborg, Sweden.
E-mail addresses: imran.hanif@chalmers.se, imran.hanif@ri.se (I. Hanif).

https://doi.org/10.1016/j.jmrt.2023.07.073

challenges as these materials are able to form Cr-rich scales that improve the high temperature corrosion resistance [7]. However, accelerated corrosion experienced in boiler environments poses challenges för high demand on corrosion resistant high-temperature materials. In order to meet these material challenges, alternative material solutions may be required to reduce the maintenance costs and increase the electrical efficiency of these plants. Iron-chromium-aluminum (FeCrAl) alloys with varying compositions are primarily used for heating elements at higher temperatures (900 °C–1400 °C) and in other industrial applications e.g., ignitors, radiant tubes and heat exchangers in furnaces, etc. [8–10]. The matrix of the FeCrAl alloys is a body-centered cubic and addition of chromium (Cr) and aluminium (Al) assist in developing a protective aluminium oxide ($Al_2O_3$) scale at high temperatures (900–1300 °C), which acts as a strong diffusion barrier providing a good oxidation/corrosion protection of the alloy [10–15]. In addition to excellent oxidation/corrosion resistance at high temperature, FeCrAl alloys have also been shown to exhibit impressive electrical and thermal properties [12]. Limited studies have been performed to explore and fully understand the material's behavior at intermediate temperatures (≤600 °C) in aggressive environments such as e.g., biomass/waste power plants. Asokan et al. [10]. has recently investigated the effect of the addition of Si in FeCrAl alloys in the mild environment (dry $O_2$ and wet $O_2$ without any salt) and reported the formation of an alumina scale at 600 °C. It was suggested that Si may increase the activity of Al while decreasing the Cr activity in the alloy [10]. Eklund et al. [16,17]. have reported on the influence of Cr and Al in FeCrAl alloys after breakaway oxidation at 600 °C. However, more work is needed in order to understand the performance of these materials at intermediate temperatures in harsh environments.

Combining corrosion and mechanical properties poses a longstanding challenge for materials selection, design, and development. It is well known that high Cr content in FeCrAl alloys causes significant embrittlement around 475 °C due to a miscibility gap [7]. The embrittlement may be mitigated by selecting an optimum Cr content in the alloy. The newly developed Kanthal® EF101 is designed with an aim to significantly reduce embrittlement while maintaining a good corrosion resistance. Another attractive and cost-effective solution is to use the alloy as a metallic coating. Overlay welding for corrosion protection is a well-established technique first developed in 1950 and is a commonly used method in industry. However, the impact of overlay weld microstructure on the corrosion mechanisms in harsh environments at elevated temperature is less known [18–20]. Varghese et al. [21]. reported on the cold metal transfer clad Ni based superalloy, Inconel 617 M and 316L stainless steel and the influence of microstructure and dilution on the mechanical and corrosion properties. More work is needed in order to understand the corrosion properties of not only bulk but also weld overlay coatings produced by lean FeCrAl alloys in harsh environment at medium high temperatures.

The aim with this work is to investigate the microstructure and its impact on high temperature corrosion resistance of weld overlay and bulk Kanthal® EF101 as well as a reference chromia forming alloy in a simulated biomass/waste-fired boiler environment for long exposures at 600 °C. This comparative study provides a microstructural characterization of multi-layered oxide scales formed after breakaway oxidation of bulk and coating material using advanced microscopic techniques in order to better understand the underlying mechanisms.

## 2. Materials and methods

### 2.1. Sample preparation

The newly developed alloy Kanthal® EF101 was supplied by Kanthal in the form of both bulk (strip) and coating, and the composition is given in Table 1. The EF101 coating was applied onto the ferritic martensitic alloy SVM12 using a weld overlay technique.

The overlay welding was performed using a mech-MIG with Pulse Multi Control technique by Fronius, with built in arc control. The welding parameters used were 179 A current, 25 V voltage and a travel speed of 300 mm/min. An argon shielding gas was used with a flow of 19 l/min. The welding overlay was produced in one layer of approximately 4 mm. A higher heat input would have been needed to produce a thinner coating, but the 4 mm thick substrate limited the heat input possible. To reduce the stresses and thereby the risk of deformation and cracking during cooling, the substrate was welded onto a 50 mm thick steel block prior to coating and subsequently removed after cooling.

The martensitic stainless steel SVM12 was developed and supplied by Vallourec and the composition is given in Table 1. The SVM12 was used as a substate for the EF101 weld overlay, as well as a reference material in the corrosion investigation. The bulk and coating coupons of EF101 were of the dimensions 20 × 10 × 2 mm and 20 × 10 × 8 mm, respectively. The bulk EF101 was ground with P800 grit SiC abrasive paper using Struers TegraPol–31 machine and was ultrasonically cleaned using acetone to remove surface contaminations. The edges of the coated coupons were painted by the Instituto Nacional De Technica Aerospace (INTA) with its proprietary slurry formulation to minimize the edge effect, which may perturb the corrosion/oxidation measurements during and after the exposures. Potassium chloride (KCl) salt (0.5–2 mg/cm$^2$) was deposited onto the specimens using a spray technique before the exposure. The specimens were weighed before and after the furnace exposures using a Sartorius micro weight balance with microgram resolution.

### 2.2. Furnace exposures

The KCl salt deposited (2 mg/cm$^2$) EF101 bulk and weld overlay coated coupons were exposed in a 5% $O_2$ + 20% $H_2O$ + $N_2$ (bal.) environment at 600 °C for 168-, 500-, 1000-, 2000- and 8000 h. A gas flow of 0.1 cm/s was maintained throughout the exposure and an alumina boat filled with 5g KCl salt was placed upstream the specimens in a three-zone silica tube furnace to reduce KCl evaporation as to maintain the deposited salt onto the specimens till the end of exposure. Less KCl salt deposited (0.5 mg/cm$^2$) specimens were also exposed for 500 h in the similar environment. All the exposures were performed in a

**Table 1 – Chemical composition of base material SVM12 and Kanthal® EF101.**

| Material | Fe | Cr | Al | C | Mn | Si | Mo | V | Ni | B | N | Co | W | Nb | others |
|---|---|---|---|---|---|---|---|---|---|---|---|---|---|---|---|
| SVM12 (wt.%) | Bal. | 10.50–12.00 | | 0.10–0.16 | 0.30–0.80 | 0.20–0.60 | 0.10–0.60 | 0.15–0.30 | 0.40 | 0.008–0.015 | 0.002–0.020 | 1.50–2.50 | 1.50–2.50 | 0.02–0.10 | – |
| Kanthal EF101 (wt.%) | Bal. | 11–14 | 3.2–4.2 | <0.08 | <0.7 | 1–2 | – | – | <0.5 | – | – | – | – | – | RE |
| Kanthal EF101 (at. %) | Bal. | 11.2–14 | 6.3–8 | <0.35 | <0.7 | 1.9–3.2 | – | – | <0.5 | – | – | – | – | – | RE |

In Table 1, the abbreviation "RE" refers to the reactive elements.

continuous manner without any interruption. Thermogravimetric analysis (mass gain) was performed after cooling down the specimens for 24-h.

Theoretical oxide thicknesses were calculated using the theoretical density change given in Equation (1) by assuming that the total mass gain originates from the density change due to the ingress of oxygen [8]:

$$\Delta\rho_{theoretical} = \rho_{M_xO_y} * \frac{M(O_y)}{M(M_xO_y)} \quad (1)$$

where $\rho_{M_xO_y}$ is the density of the oxide scale, $M(M_xO_y)$ and $M(O_y)$ are the molar masses of the oxide and of oxygen in the oxide, respectively.

### 2.3. *Broad Ion Beam (BIB) milling*

After the exposure, cross-sections of the specimens were prepared using a Leica TIC 3X Broad Ion Beam (BIB) milling system. The triple ion beam milling system produces a large 2 mm wide cross-section for analysis. The BIB machine was operated at an accelerating voltage of 8.0 keV for 5 h and 4 keV for 4 h to obtain a high quality planar and smooth cross-section for analysis in scanning electron microscopy (SEM). Due to the fragility of the oxide scale, which may easily spall off during the sample preparation, a silicon wafer was glued on top of the specimen using a Loctite 415 glue then cut into two pieces using a Minitom low-speed saw from Struers and one piece was placed in the BIB milling system.

### 2.4. *Focused Ion Beam (FIB) milling*

Focused Ion Beam (FIB) system has been used to prepare samples for the Transmission Electron Microscopy (TEM) investigations. A dual-beam Versa 3D FIB from FEI was used to prepare site-specific thin lamella from the BIB cross-sections. The FIB used in the current study was equipped with a liquid metal ion source (LMIS) of Ga and an in-situ Omniprobe needle for lift-out. A conventional FIB sample preparation method used in Ref. [22] was employed for TEM sample preparation: a protective Pt layer was deposited onto the area selected for lift-out. An accelerating voltage of 30 keV and a beam current of 30 nA was used to make trenches and a fine milling was performed using a beam current of 7 nA. After lifting out the sample in-situ using Omniprobe and welding the sample on FIB lift-out Cu grid, the lamella was thinned down using an acceleration voltage of 30 keV and a beam current of 1 nA. The acceleration voltage and beam current were subsequently lowered to 16 keV and a beam current of 30 pA. Finally, the samples were plasma cleaned via a low voltage of 2 keV argon milling using Fischione 1020 plasma cleaner system.

## 3. Analytical techniques

### 3.1. *Scanning electron microscopy and Energy Dispersive X-ray (EDX) spectroscopy*

The Scanning Electron Microscopy (SEM) investigations were performed using an FEI Quanta 200 ESEM field emission gun

machine equipped with an Oxford Instruments X-Max 80T Energy Dispersive X-ray (EDX) detector. The SEM was operated with an accelerating voltage of 20 keV for imaging and EDX analysis.

### 3.2. *Transmission electron microscopy (TEM)*

Transmission Electron Microscopy (TEM) investigations were performed using an FEI Titan 80–300. The field emission gun TITAN is equipped with an Oxford X-sight EDX detector and high-angle annular dark field (HAADF) detector. The TEM was operated in Scanning TEM (STEM) mode at 300 keV for microstructural and STEM-EDX investigations using HAADF detector. The STEM-EDX analysis were acquired normal to the probe and the data was post-processed using FEI TEM Imaging and Analysis (TIA) software.

## 4. Results

The corrosion behavior and microstructural differences between the FeCrAl alloy EF101 bulk material and weld overlay coating when exposed in KCl-rich environment is investigated in detail. The general corrosion behavior is compared with a martensitic stainless steel SVM12 while the focus is on the EF101 bulk/weld overlay. Three specimens of each bulk/weld overlay material were exposed in 5% $O_2$ + 20% $H_2O$ + $N_2$ (bal.) + KCl(s) for up to 8000 h at 600 °C. Oxide thickness measurements were carried out from representative regions on the representative parts of the very wide ion milled cross-sections. The presented results demonstrated the repeatability of the findings under same conditions.

### 4.1. *Unexposed microstructure - bulk and overlaid weld*

The microstructure of the EF101 bulk specimen was investigated using SEM on an ion-milled cross-section, see Fig. 1a. The elemental composition of EF101 given in Table 1 was verified using Energy Dispersive X-ray (EDX) spectroscopy. The material's grain size was determined from the SEM/BSE images and found to range between 11 and 40 μm. The EF101 bulk contains reactive elements, which can be seen as 1–3 μm large bright particles randomly located within the grains and across the grain boundaries, indicated with arrows in Fig. 1a.

The thickness of the weld overlay coating was approximately between 3.5 and 5.5 mm. The chemical composition of the EF101 coating was analysed using SEM-EDX spectroscopy. However, SEM-EDX quantification revealed a compositional difference between the bulk and weld overlay coating close to the coating/metal interface. The largest difference was observed near the substrate-coating interface indicating a dilution caused by interdiffusion during the welding process (a region of ~15–20 μm was affected). This resulted in a higher amount of Fe (86 at-% instead of 79 at-%) and somewhat lower amount of Al (1 at-% instead of 6 at-%), Cr (11 at-% instead of 13 at-%) at the metal-coating interface (in the SEM-EDX). However, the composition of the coating at approximately 35 μm away from the coating/metal interface contained a composition very close to the bulk composition. The REs particles were observed as 1 μm large precipitates

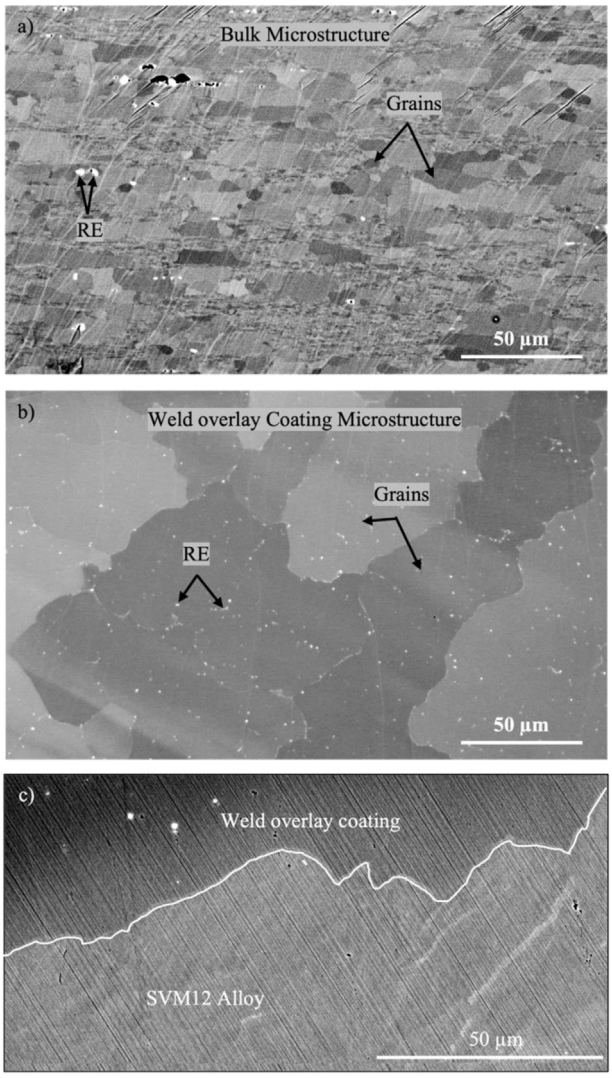


**Fig. 1 – Back scattered electron SEM micrographs illustrating the grain size of the Kanthal® EF 101 bulk (a) and weld overlay coating (b), bright precipitates are the reactive elements randomly distributed within the grains and grain boundaries. SE–SEM micrograph showing the non-uniform coating -metal interface in (c).**

preferentially located within the grain boundaries (see Fig. 1b). The microstructural investigations of the EF101 coating showed no apparent cracks or signs of porosity. A non-uniform metal-coating interface and good adhesion was observed in the optical and scanning electron microscope (SEM) as shown in the inset in Fig. 1c. The grain size was relatively uniform throughout the EF101 overlay welded coating (see Fig. 1b) and was found to range from 20 to 70 μm.

### 4.2. *Oxidation kinetics*

The mass gain data provides an estimation of the oxidation rate and is proportional to the oxide thickness [23] as Fig. 2 and section 2.2 depicts. However, some of the edges of the coating specimen were more corroded as the proprietary slurry in

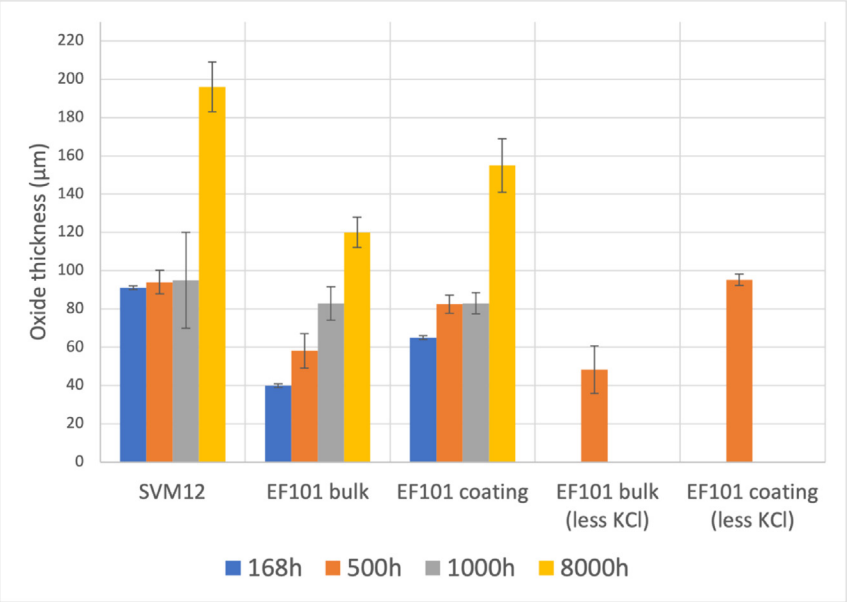


**Fig. 2 – Average measured oxide thicknesses of the Kanthal® EF101 bulk and weld overlay coating when exposed to 5% $O_2$+20%$H_2O$ + $N_2$ (bal.) under KCl rich environment for up to 8000 h at 600 °C. The oxide thickness of the reference SVM12 used as a base material for weld overlay coating is also presented.**

some cases spalled off during exposure, revealing the underlying SVM12 substrate. All oxide thicknesses were measured on SEM-BSE images of ion milled cross-sections. While the theoretical oxide thicknesses (obtained using equation (1)) were higher than the measured values, the mass gain and actual oxide thickness displayed similar trends. Fig. 2 displays the average oxide thicknesses of the reference uncoated SVM12, EF101 bulk and EF101 overlay weld for exposures of 168 h up to 8000 h at 600 °C in a KCl-rich environment. The EF101 weld overlay coatings showed higher mass gains compared to the EF101 bulk counterpart and hence also oxide thicknesses (see Fig. 2). The oxide thickness of the reference SVM12 used as a base material for weld overlay coating is also presented in Fig. 2.

The general microstructure of all exposed specimen has been reported here [24]. The general overview investigation in the referred report offered a foundation for more comprehensive microstructural investigation of the difference between bulk/weld overlay FeCrAl corrosion properties. In this study, the oxide thickness measurements for EF101 showed the same general trend for all specimen except for the 1000 h-exposure where spallation was observed, see Fig. 2. The reference martensitic SVM12 had the highest mass gain and formed a 92–130 μm thick oxide scale. The oxide scale was composed of an outward-growing iron oxide and an inward growing mixed oxide [22] This type of microstructure has been reported to form after breakaway oxidation in harsh environments in what has been referred to as the secondary corrosion regime [23]. The oxide scales formed on both EF101 weld overlay coating and bulk material grew slower than SVM12 but displayed similar general microstructure (multi-layered scale) indicating breakaway oxidation i.e., transition from the primary to the secondary corrosion regime when exposed in the presence of KCl. The remnants of KCl salt were also identified over the oxide scale in plan-view SEM image (not shown here) after 500 h exposure on all specimens.

In order to investigate the oxide microstructure in detail with the TEM, the specimens exposed for 500 h (0.5 mg/cm$^2$) were selected. All oxide features are represented and have grown larger than after 168 h exposure, while the challenge with spallation when cooling specimen/cutting cross-sections was smaller than for the longer exposures/larger amount of KCl. The overview of the oxide scale developed on the bulk EF101 after 500 h exposures in KCl environment is shown in Fig. 3a. The oxide scale was composed of an outward growing and an inward growing oxide with a total thickness of 39–69 μm. This is in line with the calculated thickness of 41 μm. The ratio of inward- and outward-growing oxide scale for the bulk EF101 was found to be approximately 1:1. The thick outward-growing oxide scale was identified as an iron oxide of approximately 26–49 μm and inward growing oxide scale was composed of mixed (Fe, Cr, Al, Si) oxide of approximately 13–20 μm.

The overview of the oxide scale developed on the EF101 coating after 500 h exposure is shown in Fig. 3b. The oxide scale was composed of an outward-growing and an inward-growing oxide with a total thickness of 66–119 μm. This is in line with the calculated thickness of 76 μm. The ratio of inward- and outward-growing oxide scale for the coated EF101 was found to be approximately 1:1. The outward-growing oxide scale was identified as an Fe-oxide with a thickness of approximately 38–57 μm and the inward-growing oxide scale was composed of mixed (Fe, Cr, Al, Si) oxide of approximately 28–62 μm.

In order to investigate the microstructure of the inward-growing part and the thin oxide layers (on the bulk/coating)

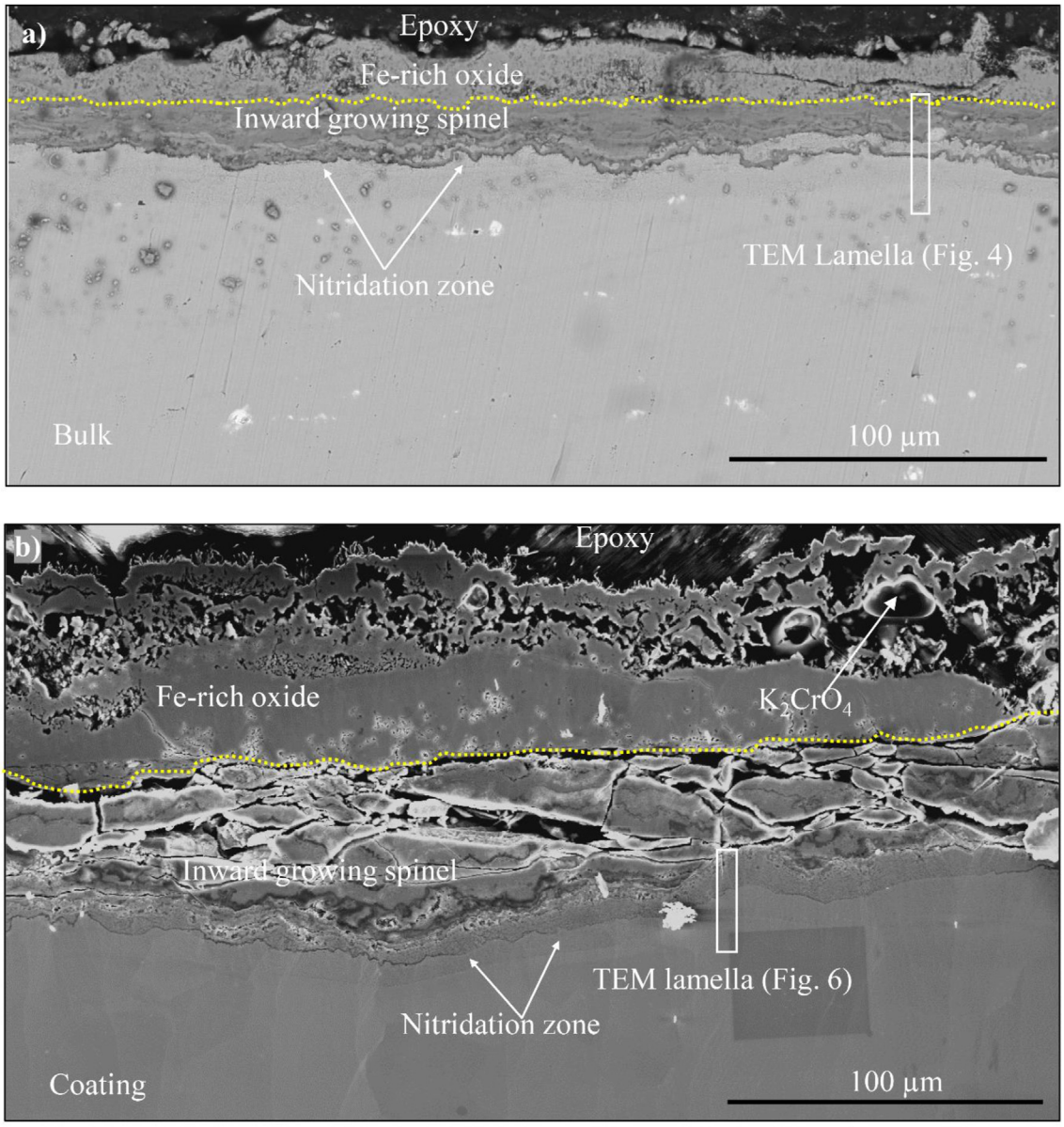


**Fig. 3 – SEM micrographs showing the backscattered image of the overview of the polished Kanthal® EF101 bulk (a) and ion milled weld overlay coating (b). The specimens were deposited with 0.5 mg/cm$^2$ KCl salt and exposed to 5%$O_2$+20%$H_2O$ + $N_2$ (bal.) for 500 h at 600 °C with a KCl boat placed upstream.**

in detail, thin foil samples were lifted out from representative areas (see indication of position in Fig. 3) and TEM investigations were performed.

### 4.3. *Detailed oxide microstructure - bulk and overlaid weld EF101*

The preliminary microstructural characterizations showed that the outward growing oxide scales were Fe-rich (98 at-% Fe, cations or more) on both the EF101 bulk and coating. The inward-growing scale was shown to consist of a complex (Fe, Cr, Al, Si)-oxide scale in both cases. Indications of a nitridation zone could be observed in the region just below the inward-growing scale to same depth for both cases. Reactive elements could be identified on the SEM micrographs of the cross-section with the same size and distribution both prior to and post exposures. The detailed microstructural investigation is focused on the complex inward-growing (Fe, Cr, Al, Si)-oxide scales and the alloy just below the scale as previous research indicate that this part may provide vital information about the corrosion resistance of the coating/bulk specimens.

### 4.4. *Detailed microstructural investigation of inward growing scale (bulk)*

A detailed TEM investigation of the bulk EF101 was carried out to understand the nature of the complex inward-growing scale formed during secondary oxide. The inward-growing oxide

scale formed on the bulk EF101 was thick and undulating and special attention was put on selecting a representative region for FIB milling/TEM lift-out, see marked region in Fig. 3a.

Fig. 4 shows a high-angle annular dark field (HAADF) image of the thin lamella. The top layer was identified as the outward growing iron oxide formed on top of the inward growing oxide layer. The region (I–II) underneath the Fe-oxide was identified as an inward-growing oxide. The chemical composition of the 1.5–2.5 μm thick region (I) was found to be 12 at-% Fe, 42 at-% Cr, 35 at-%, Al and 10 at-% Si. In addition, small amounts of K were also detected in this region. The 5 μm thick region II can be divided into two sub-regions i.e., undulating dense and porous regions. The elemental distribution in the inward growing layer was of about 15–20 at-% Fe, 30–55 at-% Cr,

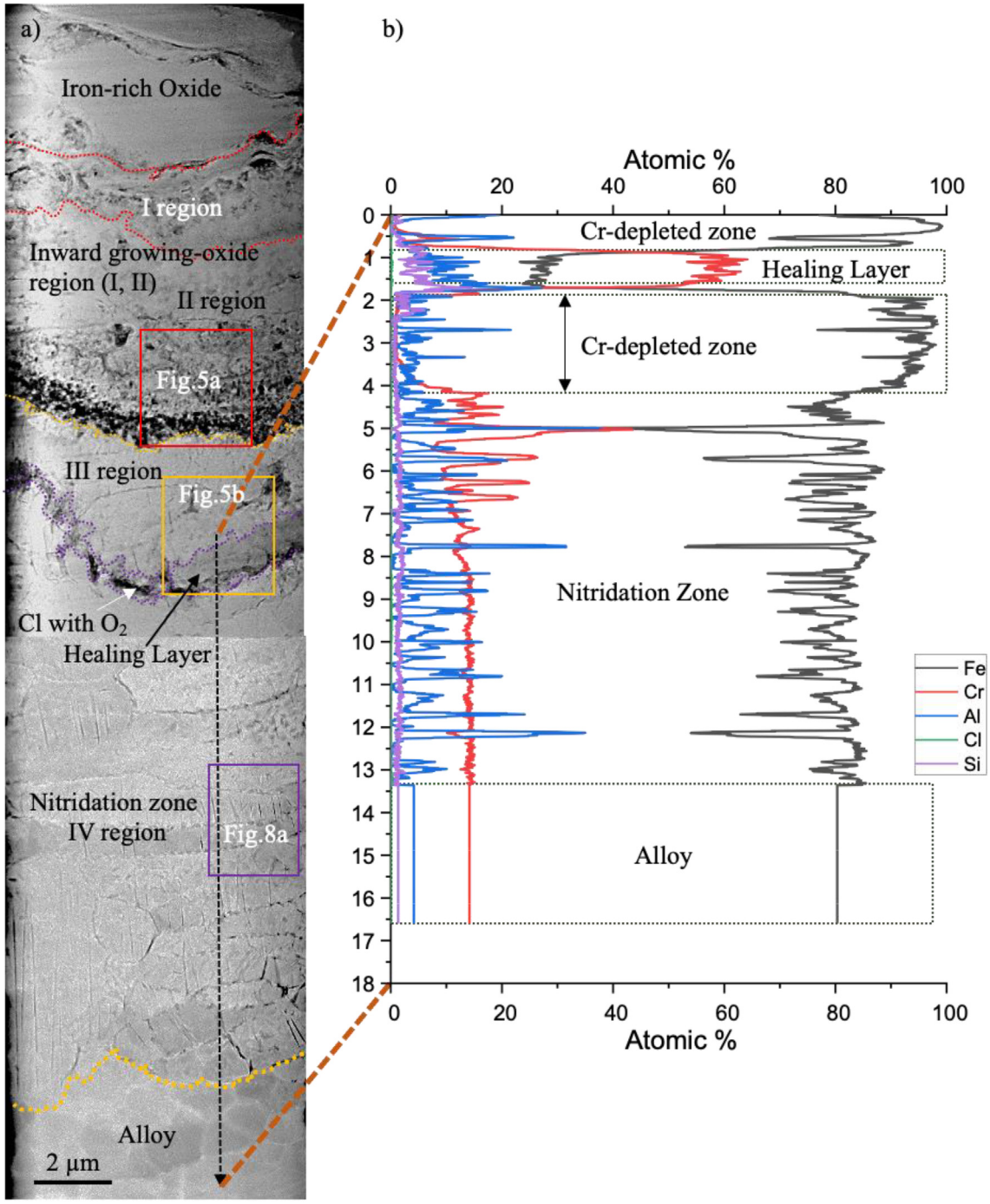


**Fig. 4 – HAADF-STEM images showing an overview of the bulk Kanthal® EF101 thin lamella (a) representing the multi-layered oxide when exposed to 5%$O_2$+20%$H_2O$ + $N_2$ (bal.) under KCl rich environment for 500 h; STEM-EDX line scan profile is presented in (b) revealing the presence of a healing layer of about 1 μm (Cr + Al ≥ 70 at-%) and 2 μm deep depletion zones of Cr after the healing layer. AlN zone of 12–16 μm deep could be identified. The dashed arrow marks the area and direction of the STEM-EDX line scan.**

20–30 at-% Al, 5–15 at-% Si. The porous region of the inward growing oxide was composed of grey and dark contrasts (see Fig. 5c) corresponding to an Fe/Al-rich oxide with an average composition of 60 at-% Fe, 3 at-% Cr, 33 at-% Al, and 4 at-% Si. One phase (light grey) was slightly higher in Si and Cr compared to the dark phase, see Fig. 7c. Region III was identified as an unoxidized segment of the alloy (1.5–3 μm) and the STEM-EDX analysis showed that the region was depleted in Cr and rich in Fe (95 at-%) with Al (3 at-%) and Si (2 at-%).

The middle region with a dark contrast underneath the unoxidized zone was identified as a re-passivated layer and the STEM-EDX quantification analysis indicate this dark layer may be a corundum-type oxide scale, based on the total amount of trivalent ions (Cr + Al being higher than 67% cations). This re-passivated layer is named "healing layer" in this paper and the average chemical composition was found to be 59–65 at-% Cr, 26–30 at-% Fe, 3–10 at-% Al and 1–2 at-% Si. A small increase of Cl (in the range of 1 at-% Cl) was identified in surrounding regions of the healing layer. Approximately 2 μm of the alloy beneath the healing layer was depleted in Cr. The region named IV with dark bands of varying lengths underneath the healing layer was identified as nitridation zone consisting of Al nitrides in the range of 300–650 nm, seen in Fig. 8a. The depth of the nitridation zone varied between 12 and 16 μm. The alloy below the nitridation zone maintained the original composition, grain size and reactive elements.

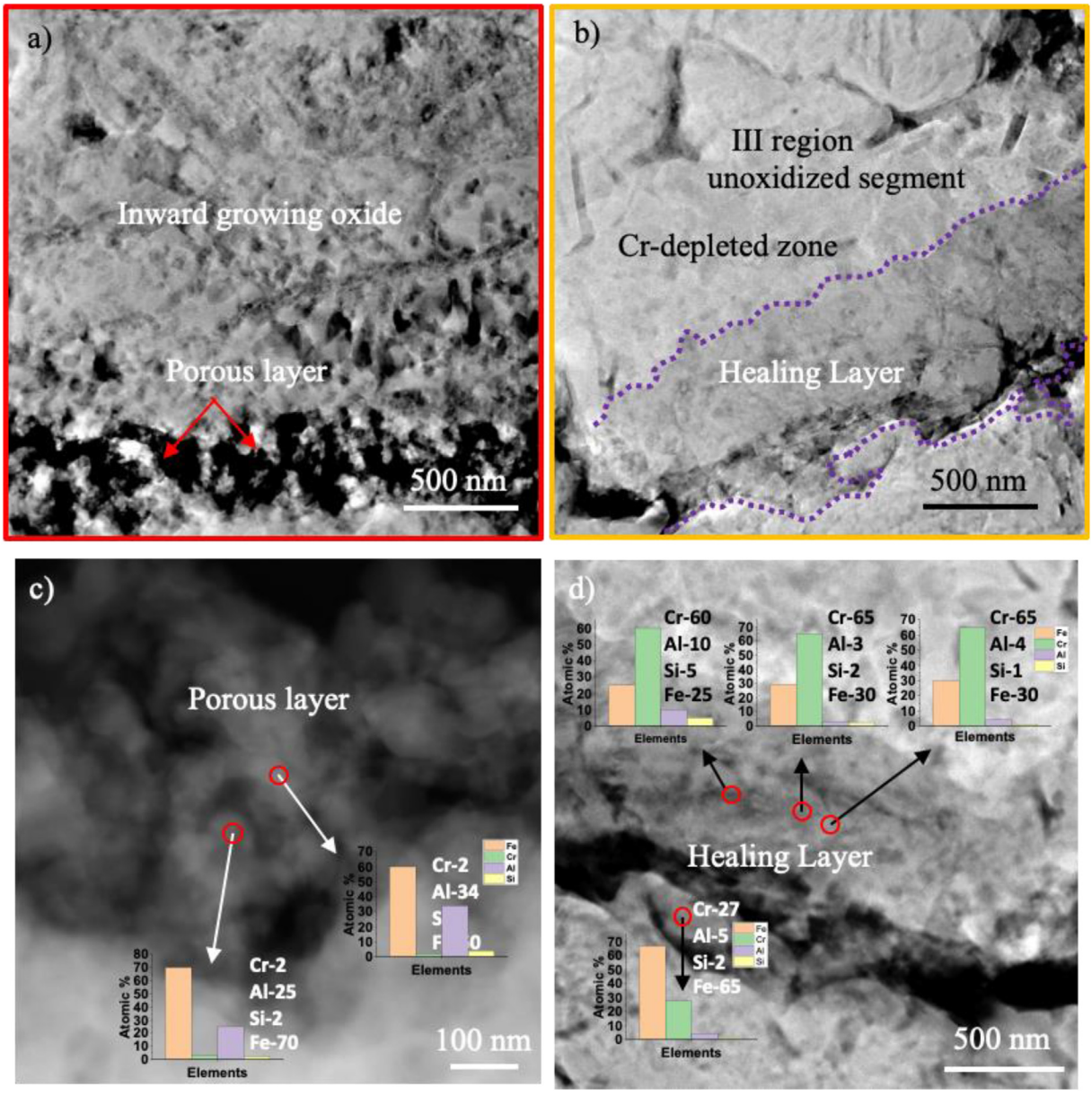


**Fig. 5 – HAADF-STEM micrographs (a and b) of the areas marked with red and yellow squares in Fig. 4. High magnification image of the porous (c) and the healing layer (d) with bar graphs in insets representing the STEM-EDX quantification performed at different points.**

### 4.5. *Detailed microstructural investigation of inward growing scale (weld)*

A detailed TEM investigation of the EF101 coating was carried out in a similar manner to the bulk EF101. A thin foil sample was lifted out from a representative region of the BIB cross-section covering the inward-growing oxide scale and part of the alloy. The focus was put on the corrosion front in the thick inward-growing scale in order to complement the SEM/EDX analysis. This type of region is marked with a rectangle in Fig. 3b. An overview of the thin lamella of the EF101 coating is shown in the HAADF micrograph in Fig. 6. Point analysis and line scans were carried out using STEM-EDX for quantification and elemental distribution within the inward-growing scale.

The uppermost layer was identified as a non-uniform inward-growing oxide with a thickness of approximately

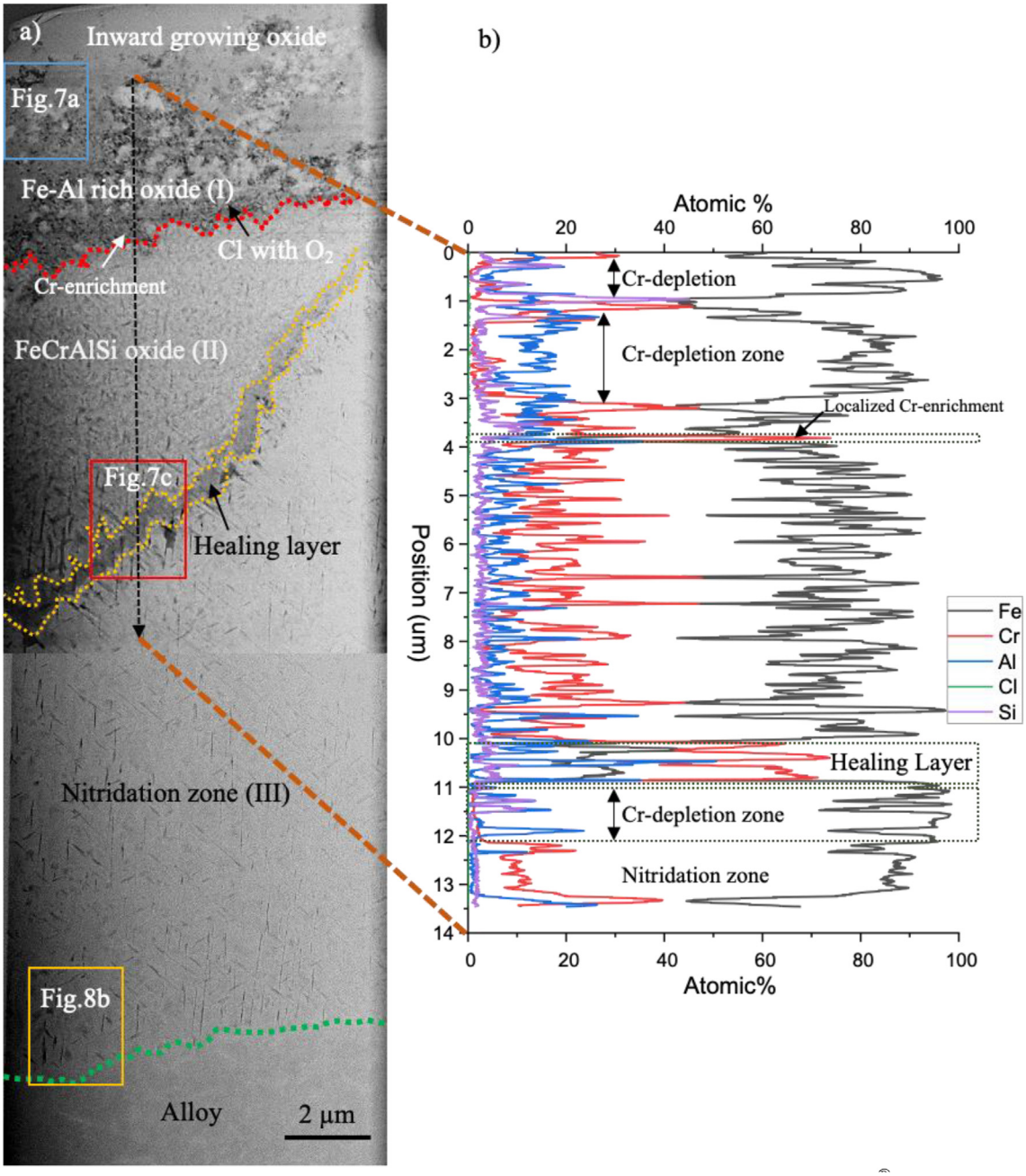


**Fig. 6 – HAADF-STEM images show an overview of the thin lamella of Kanthal® EF101 weld overlay coating (a) representing the multi-layered oxide when exposed to 5%$O_2$+20%$H_2O$ + $N_2$ (bal.) under KCl rich environment for 500 h at 600 °C; STEM-EDX line scan profile is presented in (b) revealing the presence of 1 μm and 2 μm thick depletion zones of Cr within the complex inward growing oxide scale and around 1 μm thick depletion zone of Cr after the healing layer. A 1 μm thick healing layer (marked in yellow) with Cr + Al ≥ 67 at-% was also identified. AlN zone of 10–17 μm deep could be identified. The dashed arrow marks the area and direction of the STEM-EDX line scan.**

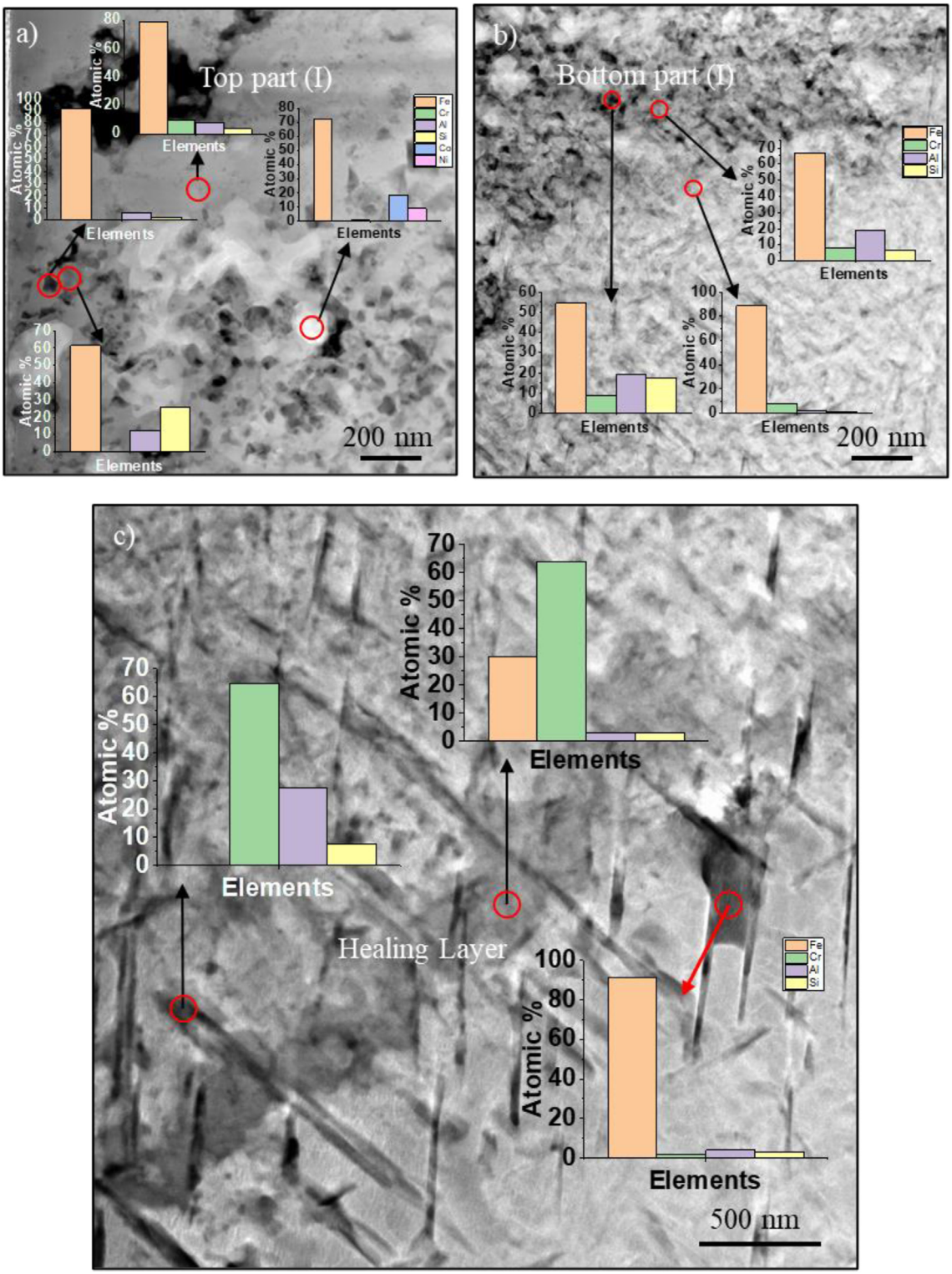


**Fig. 7 – HAADF-STEM micrographs showing the high magnification images (a, b) of the complex inward growing oxide layer (region-I) and a healing layer (c) developed on the Kanthal® EF101 weld overlay coating when exposed to 5%$O_2$+20% $H_2O$ + $N_2$ (bal.) under KCl rich environment for 500 h at 600 °C. The chemical composition at local spots marked with red arrows is presented in the insets with column bars.**

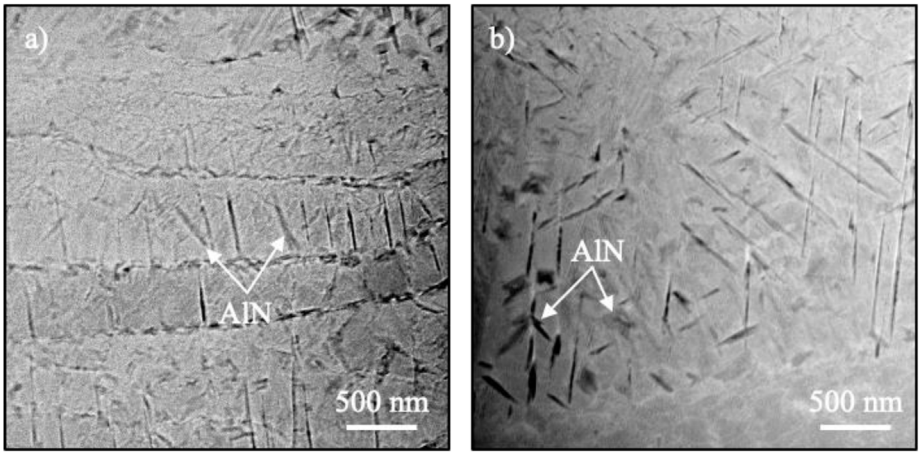


**Fig. 8 – HAADF-STEM micrographs showing the AlN zones in Kanthal® EF101bulk (a) and weld overlay coating (b).**

5.5–13 μm. The inward-growing oxide scale could be divided into two regions: a top region (I) with a grey contrast, bright nodules, pores and dark regions and a region with dark bands (II). High magnification HAADF micrographs illustrating the morphology of the complex inward-growing oxide scale can be seen in Fig. 7. The 5.5 μm thick region I was identified as an Fe/Al-rich oxide and elemental distribution was of about 50–90 at-% Fe, 15–20 at-% Al, 8–20 at-% Cr and 5 at-% Si. In addition, the quantification data shows that the light-grey phase has 62 at-% Fe, 12 at-% Al, and 27 at-% Si and the dark phase as iron-rich with 92 at-% Fe and 6 at-% Al. The size of the bright nodules present in the top part (I) of the inward-growing oxide scale (see Fig. 7a) varies from 100 to 400 nm and the STEM-EDX point analysis identified them as un-oxidized intermetallic phases of 72–88 at-% Fe, 10–18 at-% Co and 1–9 at-% Ni. Since the EF101 does not contain Co and no Ni, it could be assumed that those elements come from the substrate-SVM12 during the coating manufacturing process. Low amounts of Cl was also identified in the bottom of the porous region (I). A Cr depleted zone of 1 μm thick was identified below the healing layer, see Fig. 6, where the Cr-concentration varied from 2 to 8 at-%. In addition, localised Cr-enrichment at the I/II region interface was also identified, where the Cr concentration was around 40–65 at-%, see line scan in Fig. 6. The bottom part of the inward-growing oxide II region, approximately 2–7.5 μm thick, was composed of grey and dark phases. The average chemical composition within this zone was found to be around 70 at-% Fe, 17 at-% Cr, 8 at-% Al and 5 at-% Si. The composition of the grey phase was of about 67% Fe, 20 at-% Al, 8 at-% Cr, 5 at-% Si. The dark phase constitutes less iron- 55 at-% Fe, 20 at-% Al, 10 at-% Cr and high- 15 at-% Si.

The middle region with an undulating dark layer was identified as a re-passivated layer (healing layer). The STEM-EDX quantification analysis revealed the average chemical composition of the healing layer to be 64 at-% Cr, 30 at-% Fe, 3 at-% Al and 3 at-% Si and indicate this dark layer may be a corundum-type oxide (based on the total amount of trivalent ions (Cr + Al being ≥67 at-% cations). In contrast to the bulk EF101, no Cl was detected in the surroundings of the healing layer. The III region, with dark bands, underneath the healing layer was identified as a nitridation zone with Al nitrides in the range of 150–550 nm, see Fig. 8b. The depth of the nitridation zone varied between 10 and 17 μm. The coating followed the nitridation zone with an original composition, grain size and reactive elements.

## 5. Discussion

### 5.1. *General observations*

In order to better understand the potential of the lean FeCrAl alloys in harsh environments, the behavior following breakaway oxidation needs to be studied in detail for long durations. It is in addition important to recognize the corrosion protection of different types of material solutions, i.e., bulk/coating, as one obvious way is to use the material as solid bulk material/tube or as a compound tube. Another pathway is to use the alloy composition as a metallic coating [25–28]. In this work the material Kanthal® EF101 (lean FeCrAl alloy) was selected, and the corrosion protection compared to the SVM12 (ferritic-martensitic stainless steel) in harsh environments.

The main objective with this investigation was to compare the properties of the bulk material and weld overlay coating when both have a similar chemical composition. SEM-EDX quantification for the EF101 bulk was in good agreement with the stated alloy composition given in Table 1 while a dilution was observed for the weld overlay coatings close to the coating-metal interface (a region beginning at the coating-metal interface and ending at a distance of 35 μm from this interface). The compositional difference for the coating specimen may arise mainly due to the overlay welding process where the substrate material mixes with the coating which may influence the composition of the coating. Dilution [29–31] is a well-known phenomenon caused by the metallurgical bond between the substrate and coating. An increased dilution is observed at the coating-metal interface and significantly reduced effect was observed far away from the interface and close to the surface the composition is in line

with the bulk composition. The result is in accordance with earlier reported studies [30,32,33] and multi-layered deposition/welds could significantly reduce the effect of dilution [30]. Nevertheless, since the dilution only affected about 35 μm of the entire coating thickness, the influence of dilution on the corrosion behavior is expected to be minor. The relatively low dilution in this study may be explained by the chemical composition of substrate and coating being similar (both Fe-based). A higher dilution would be expected in the case of a Ni-base/Fe-base coating/substrate system., see e.g., Ref. [34].

In addition to the small difference in composition a large difference in grain size was observed comparing the bulk and coating microstructure, see Fig. 1. The difference in grain size of the bulk and coated material is influenced by the heat treatment during the manufacturing process where the strip for bulk material has been hot and cold worked and then subsequently heat treated leading to a microstructure with fine grains due to recrystallisation. For the overlay welded coupons, the wire was melted and resolidified resulting in a microstructure with coarse grains. Leonardo et al. [30]. and Kucita et al. [31] have reported that dilution in the metallic coatings not only impacts the chemical composition but also strongly influence the microstructure and mechanical properties.

Breakaway triggered by breakdown of the primary protection (Cr/Al-rich oxide scale) is a well-established phenomenon at high temperature in harsh environments and was also observed in the present work. The breakdown of the primary protection in FeCrAl alloys at 600C in the presence of KCl has already been reported [10,13,35–38] and attributed to either the Cr-depletion [39,40] due to chromate formation or Cl-induced corrosion [41,42]. In the present study, both the EF101 bulk and coating transitioned into a secondary corrosion regime (i.e., corrosion after breakaway oxidation) already after the shortest exposure time (168 h) and was in the secondary mode during all exposures from 168 to 8000 h. This is consistent with the earlier work performed by Eklund et al. [16] reporting a very short incubation time or rapid transition of FeCrAl alloys from the primary to secondary corrosion regime in the presence of KCl. Following breakaway oxidation, i.e. secondary regime, all specimens developed a multi-layered oxide scales consists of an outward-growing Fe-oxide and a complex inward-growing oxide scale in all cases (see Fig. 3) indicating diffusion-controlled growth. All mass gain and thickness measurements in addition indicate parabolic growth rates, i.e. diffusion controlled growth kinetics. Despite the presence of Cl in the scale, no signs of active oxidation could be observed [43]. This is in line with only small amounts detected in the microstructure of the corrosion products in all cases.

### 5.2. *Influence of oxide microstructure – secondary protection*

The microstructure/composition of the outward-growing Fe-rich oxide scale was found to be similar for the reference material SVM12 as well as for both EF101 bulk and coating. The observed trend is consistent with the findings reported in earlier studies [7,22,44], i.e. an oxide microstructure consisting of an outward-growing iron oxide scale following breakaway oxidation in different environments. This implies diffusion-controlled kinetics (in line with the parabolic growth rate) where the diffusivity of Fe is much higher in the inward-growing spinel than other alloying elements i.e. Cr and Al, resulting in an outward growing almost pure iron oxide scale [45,46]. The current work is therefore focused on a detailed investigation of the complex inward-growing oxide scale developed after 500 h of exposure with less KCl as the outward-growing scale may not explain the observed differences in oxidation kinetics/corrosion resistance. Especially, the focus is set on the bulk/weld specimens as the trend regarding corrosion protection in harsh environments has been reported before for several material systems [7]. The SVM 12 alloy oxidation kinetics and microstructure do not show any signs of a good secondary protection while this is not investigated in detail, see Fig. 2. Several investigations have in addition reported the microstructure of a poor secondary protections in detail, see e.g., Refs. [47,48].

The advanced TEM analysis shows the very complex microstructure of the inward-growing scale in detail, see Figs. 4–7. Close to the original alloy surface, possible signs of an early formed healing layer were identified on EF101 bulk as a separate layer with a concentration of 77 at-% cations (Al and Cr). Below this layer the inward-growing oxide scale continues. On the other hand, the EF101 coating exhibited no indications of formation of an early healing layer in the upper part of the inward-growing scale. This may be explained by a better supply of Cr to the surface for the bulk alloy (facilitated by smaller alloy grains) through alloy grain boundaries (see Fig. 1a and b). This was supported by a lower Cr concentration for the bulk material compared to the coating in this region below the possibly early formed healing layer in the upper part of the inward-growing oxide. The inward-growing oxide scale formed on both the EF101 bulk and coating was composed of dense and porous regions with very complex microstructure. However, the key differences were identified as local composition indicating the protective part of the inward growing-oxide as well as a depletion zone below the healing layer and thickness of healing layer, see Table 2. It may be noted that the weld overlay coating in addition contained bright intermetallic nodules (containing elevated amounts of Co and Ni) within the top part of the inward growing oxide scale, see Fig. 6. However, this is not expected to influence the corrosion resistance significantly because of the sparsity of these phases.

One of the key features of a good secondary protection is a dense slow growing oxide scale. Indications of such as scale may be found in both bulk and coating systems, see Figs. 4 and 6. This layer may be referred to as a healing layer having a high Cr-concentration along with Al. The composition of the healing layer suggests a corundum-type oxide scale for EF101 bulk and mixed phases of spinel and corundum for the coating. The concentration of trivalent cations (Cr + Al) > 67 at-%) in the healing layer exceeds the maximum theoretical value for a spinel crystal structure ($(M^{+2} + M_2^{+3})O_4$), which limits the maximum concentration of divalent ions occupied in the tetrahedral site and trivalent ions occupied in the octahedral sites to 33.3 at-% and 67.7 at-%, respectively [49]. Identification of this corundum type Cr/Al-rich layer after breakdown of the primary protection has previously been reported in other

**Table 2 – Key microstructural differences in the Kanthal® EF101 bulk and weld overlay coating after exposed in 5%$O_2$+20% $H_2O$ + $N_2$ (bal.) under KCl-rich environment for 500 h at 600 °C.**

| Feature | Bulk | Weld overlay coating |
|---|---|---|
| Potassium chromate in deposit/ oxide interface | No apparent | $K_2CrO_4$ |
| Oxide porosity outward growing scale (iron oxide) | YES | YES |
| *I Region (Cr/Al rich scale)* | 1–2 μm thick with a composition indicating corundum (42 at-% Cr, 35 at-% Al and 11 at-% Si) | No indications |
| Cr/Al/Si-content–inward growing scale | II Region-Dense: 35 at-% Cr, 25 at-% Al and 10 at-% Si<br>II Region-Porous (1.7–3 μm): 60% Fe, 3 at- % Cr, 33 at-% Al, and 4 at-%.Si<br>III Region-unoxidized segment (1.5–3 μm): 0.5 at-% Cr, 95 at-% Fe, 2.5 at-% Al, 1.5–2 at-% Si | Fe/Al rich oxide (I) (5.5 μm thick): 50–90 at-% Fe, 15–20 at-% Al,<br>8–20 at-% Cr and 5 at-% Si<br>FeCrAlSi oxide (II) (1.7–7.5 μm thick):<br>70 at-% Fe, 15–20 at-% Cr, 8 at-% Al and 5 at-% Si |
| ***Healing layer*** (Cr/Al rich layer in bottom of the inward- growing scale) | ***Thickness:* 1–1.2 μm**<br>Composition: 60–65 at-% Cr, 25–30 at-% Fe, 4–10 at-% Al and 1–2 at-% Si | ***Thickness:* 300–500 nm**<br>Composition: 60–65 at-% Cr, 30–40 at-% Fe, 3–5 at-% Al and 2–5 at-% Si |
| ***Cr-depletion zone*** (beneath the healing layer) | ***Length*: 2 μm** | ***Length*: 1 μm** |
| Presence of Cl | Traces of Cl (less than 1 at.%) | Traces of Cl (less than 1 at.%) |
| Nitridation Zone (NZ) | Depth: 12–16 μm<br>Size: 300–650 nm | Depth: 10–17 μm<br>Size: 150–550 nm |
| ***Alloy Grains*** | ***Small grains*-11–40 μm** | ***Large grains*-20–70 μm** |
| Reactive elements | 1–3 μm: within alloy grain and across the GB | 1 μm: preferentially within GB |

studies [16,35,44,50]. In a recent study by Eklund et al. [16]. a 0.5–2 μm thick highly Cr-enriched layer (exceeding the theoretical limit of trivalent ions) was observed on a Fe20CrAlSi model alloy after being exposed for 48 h at 600 °C in a KCl-rich environment. The Cr/Al-enrichment in the inward growing oxide scale was linked to the transition from a fast growth to a slow growth. However, a spinel crystal structure was identified within this layer with CBED which indicates that there may be a kinetic aspect regarding the formation of a continuous corundum-type healing layer due to phase transformation from a spinel phase in combination with diffusion of Cr from the bulk below. The phase transition to form a continuous corundum-type layer is further supported by the fact that the Cr-rich layer grows considerably faster than a chromia scale for which the slow growth (50–70 nm after 24 h [49]) and (70–90 nm after 168 h [36]) has been reported for Fe10–25Cr when exposed in a dry $O_2$ at 600 °C. Nevertheless, the enrichment of Cr/Al and/or the partial transformation from Cr-rich spinel to Cr-rich corundum-type oxide may significantly reduce diffusion through the scale without necessarily forming a continuous healing layer. It may be noted that a highly Cr-enriched layer at the metal oxide interface needs a supply of Cr from the alloy in addition to the loss of Fe through outward diffusion. This is consistent with the identified Cr-depleted zones of 2 μm and 1 μm beneath the healing layer for both EF101 bulk and coating respectively, see STEM-EDX line scans in Figs. 4 and 6. The depletion zones of Cr/Al identified below the corrosion front in the surrounding alloy may have been formed during the growth of healing layer and the slow-growing inward growing oxide. Since the bulk EF101 contains smaller grains, this may support faster diffusion along grain boundaries compared to the EF101 weld overlay coating resulting in the observed compositional differences in the secondary protection regime and varied length of depletion zones. The ability of the alloy to transition into a protective secondary mode may rely on the ability to provide Cr/Al to the growing scale as well as the activity of Cr/Al [44].

Nitridation zones of varying thickness, 12–16 μm and 10–17 μm, were observed in EF101 bulk and coating, respectively. The nitrides have been identified as AlN. Nitridation zones are considered less favorable in materials and may cause brittleness and could potentially deplete the alloy matrix in Al, which is required to form alumina [51]. The transportation of $N_2$/N is still not a fully understood phenomenon but reportedly diffuse along the oxide grain boundaries [52]. The size of the AlN observed in the EF101 bulk was 300–650 nm which is larger than the coating counterpart, varying from 150 to 350 nm indicating a faster diffusion of $N_2$ for the bulk material in line with the earlier results. However, as both microstructures show signs of improved corrosion resistance after longer times the results indicate that the formation of AlN does not limit the secondary protection on the FeCrAl alloys in harsh environments while the nitride formation may influence the mechanical properties of the alloys.

## 6. Conclusion

- The newly developed lean FeCrAl alloy Kanthal® EF101 improves the corrosion resistance in harsh environments (KCl) at 600 °C compared to the reference SVM12 for up to 8000 h.
- The bulk alloy provides a better secondary protection, i.e. corrosion resistance after breakaway oxidation than the weld overlay coating.
- The microstructure has been characterized in detail using TEM/STEM-EDX and shows a microstructure consisting of an

outward growing Fe-based oxide and a complex (FeCrAlSi) inward growing oxide for both bulk/weld specimens.

- Cr-enrichment in the inward-growing scale is important for secondary protection as it enables the formation of a healing layer.
- The lower oxide thickness of the bulk EF101 compared to the coated EF101 may be connected to smaller alloy grain size for the former, enabling faster diffusion of Cr and facilitating the formation of a more protective Cr-rich scale.
- Cr-depletion zones were identified in the bulk and weld overlay coating.
- The results indicate that formation of Al nitrides does not influence the secondary protection. However, further studies are needed to understand the mechanism of formation and influence on material degradation at high temperatures.
- The observed oxidation behavior can be relevant in the development of more efficient coatings and material processing by considering not just the composition of the coatings but also the microstructure.

## Data availability

The raw/processed data required to reproduce these findings cannot be shared at this time due to technical or time limitation.

## Funding

This research was funded by EC, European Commission for financial support within the frame of the Horizon 2020 project "Lowering Costs by Improving Efficiencies in Biomass Fueled Boilers: New Materials and Coatings to Reduce Corrosion (BELENUS)", Grant Agreement number: 815,147.

## Declaration of competing interest

The authors declare the following financial interests/personal relationships which may be considered as potential competing interests: Torbjorn Jonsson reports financial support was provided by Chalmers University of Technology.

## Acknowledgements

This work was carried out at the High Temperature Corrosion Centre (HTC) at Chalmers University of Technology. This work was performed in part at the Chalmers Material Analysis Laboratory, CMAL.

## REFERENCES

[1] Ioannis T, Wouter N, Dalius T, Pablo RC. Towards net-zero emissions in the EU energy system by 2050. 2020. https://doi.org/10.2760/081488.

[2] United Nations-Climate Actions. https://www.un.org/en/climatechange/net-zero-coalition. [Accessed 28 September 2022].

[3] Eklund J, Paz MD, Jönsson B, Liske J, Svensson JE, Jonsson T. Field exposure of FeCrAl model alloys in a waste-fired boiler at 600°C: the influence of Cr and Si on the corrosion behaviour. Mater Corros 2019;70:1476–85. https://doi.org/10.1002/maco.201810618.

[4] Johansson L-G, Svensson J-E, Skog E, Pettersson J, Pettersson C, Folkeson N, et al. Critical corrosion phenomena on superheaters in biomass and waste-fired boilers. J Iron Steel Res Int 2007;14:35–9. https://doi.org/10.1016/S1006-706X(08)60048-5.

[5] Ma W, Zeng S, Wenga T. High temperature corrosion mechanism of Ni–5W–6B–28Cr–13Al alloy in simulated MSW incineration environment. J Mater Res Technol 2023;22:1048–64. https://doi.org/10.1016/j.jmrt.2022.11.175.

[6] Hagarová M, Baranová G, Jablonský G, Bulko B, Vojtko M, Komanický V, et al. Influence of flowing water vapor containing environment on high-temperature behavior of 9Cr creep-resistant steels. J Mater Res Technol 2023;23:3840–55. https://doi.org/10.1016/j.jmrt.2023.01.206.

[7] Persdotter A, Eklund J, Liske J, Jonsson T. Beyond breakaway corrosion – influence of chromium, nickel and aluminum on corrosion of iron-based alloys at 600 °C. Corrosion Sci 2020;177:108961. https://doi.org/10.1016/j.corsci.2020.108961.

[8] Götlind H, Liu F, Svensson J-E, Halvarsson M, Johansson L-G. The effect of water vapor on the initial stages of oxidation of the FeCrAl alloy kanthal AF at 900 °C. Oxid Metals 2007;67:251–66. https://doi.org/10.1007/s11085-007-9055-0.

[9] Liu F, Josefsson H, Svensson J-E, Johansson L-G, Halvarsson M. TEM investigation of the oxide scales formed on a FeCrAlRE alloy (Kanthal AF) at 900°C in dry O 2 and O 2 with 40% H 2 O. Mater A T High Temp 2005;22:521–6. https://doi.org/10.1179/mht.2005.062.

[10] Asokan V, Eklund J, Bigdeli S, Jonsson T. The influence of Si on the primary protection of lean FeCrAl model alloys in O2 and O2+H2O at 600 °C—a microstructural investigation. Corrosion Sci 2021;179:109155. https://doi.org/10.1016/j.corsci.2020.109155.

[11] Gulbransen EA, Andrew KF. Oxidation studies on the iron-chromium-aluminum heater alloys. J Electrochem Soc 1959;106:294. https://doi.org/10.1149/1.2427333.

[12] Field KG, Snead MA, Yamamoto Y, Terrani KA. Handbook on the material properties of FeCrAl alloys for nuclear power production applications (FY18 version: revision 1). TN (United States): Oak Ridge; 2017. https://doi.org/10.2172/1474581.

[13] Chen H, Kim SH, Long C, Kim C, Jang C. Oxidation behavior of high-strength FeCrAl alloys in a high-temperature supercritical carbon dioxide environment. Prog Nat Sci: Mater Int 2018;28:731–9. https://doi.org/10.1016/j.pnsc.2018.11.004.

[14] Chen G, Yang H, Sun H, Wang F, Wang H, Kong Q, et al. Corrigendum to "Exploring the high-temperature steam oxidation behaviors of the lean-Cr (7–10 wt%) FeCrAl alloys". S0010938X21006958 Corrosion Sci 2022;194:109927. https://doi.org/10.1016/j.corsci.2021.109927.

[15] Lipkina K, Hallatt D, Geiger E, Fitzpatrick BWN, Sakamoto K, Shibata H, et al. A study of the oxidation behaviour of FeCrAl-ODS in air and steam environments up to 1400 °C. J Nucl Mater 2020;541:152305. https://doi.org/10.1016/j.jnucmat.2020.152305.

[16] Eklund J, Hanif I, Bigdeli S, Jonsson T. High temperature corrosion behavior of FeCrAlSi model alloys in the presence of water vapor and KCl at 600 °C – the influence of Cr content. Corrosion Sci 2022;198:110114. https://doi.org/10.1016/J.CORSCI.2022.110114.

[17] Persdotter A, Eklund J, Liske J, Jonsson T. Beyond breakaway corrosion – influence of chromium, nickel and aluminum on corrosion of iron-based alloys at 600 °C. Corrosion Sci 2020:177. https://doi.org/10.1016/J.CORSCI.2020.108961.
[18] Mohammadi Zahrani E, Alfantazi AM. Hot corrosion of Inconel 625 wrought alloy and weld overlay on carbon steel by gas metal arc welding in 47 PbSO4-23 ZnO-13 Pb3O4-7 PbCl2-5 CdO-5 Fe2O3 molten salt mixture. Corrosion Sci 2021;183:109348. https://doi.org/10.1016/j.corsci.2021.109348.
[19] Guo PL, Ling LG. Effect of post-weld heat treatment (PWHT) on the intergranular corrosion of ENiCrFe-7 weld overlay cladding materials. J Mater Res Technol 2020;9:8636–45. https://doi.org/10.1016/j.jmrt.2020.05.101.
[20] Mohammeda R, Kumarb EN, Ramb GDJ, Kamarajb M, Reddyd GM, Raoc KS. Microstructure, mechanical and corrosion behaviour of weld overlay cladding of DMR 249A steel with AISI 308L. Mater Today Proc 2019;15:2–10. https://doi.org/10.1016/j.matpr.2019.05.017.
[21] Varghese P, Vetrivendan E, Dash MK, Ningshen S, Kamaraj M, Kamachi Mudali U. Weld overlay coating of Inconel 617 M on type 316 L stainless steel by cold metal transfer process. Surf Coat Technol 2019;357:1004–13. https://doi.org/10.1016/j.surfcoat.2018.10.073.
[22] Phother-Simon J, Hanif I, Liske J, Jonsson T. The influence of a KCl-rich environment on the corrosion attack of 304 L: 3D FIB/SEM and TEM investigations. Corrosion Sci 2021;183:109315. https://doi.org/10.1016/j.corsci.2021.109315.
[23] Berthod P. Kinetics of high temperature oxidation and chromia volatilization for a binary Ni–Cr alloy. Oxid Metals 2005;64:235–52. https://doi.org/10.1007/s11085-005-6562-8.
[24] Ssenteza V, Eklund J, Hanif I, Liske J, Jonsson T. High temperature corrosion resistance of FeCr(Ni, Al) alloys as bulk/overlay weld coatings in the presence of KCl at 600 °C. Corrosion Sci 2023;213:110896. https://doi.org/10.1016/J.CORSCI.2022.110896.
[25] Sadeghimeresht E, Markocsan N, Huhtakangas M, Joshi S. Isothermal oxidation of HVAF-sprayed Ni-based chromia, alumina and mixed-oxide scale forming coatings in ambient air. Surf Coat Technol 2017;316:10–21. https://doi.org/10.1016/j.surfcoat.2017.03.017.
[26] Presuel-Moreno F, Jakab MA, Tailleart N, Goldman M, Scully JR. Corrosion-resistant metallic coatings. Mater Today 2008;11:14–23. https://doi.org/10.1016/S1369-7021(08)70203-7.
[27] Hiyam F. Operation, maintenance, and repair of land-based gas turbines. Elsevier; 2021. https://doi.org/10.1016/C2019-0-02860-9.
[28] Ramesh S. Corrosion Control for offshore structures. Elsevier; 2014. https://doi.org/10.1016/C2012-0-01231-8.
[29] Balasubramanian V, Lakshminarayanan AK, Varahamoorthy R, Babu S. Application of response surface methodolody to prediction of dilution in plasma transferred arc hardfacing of stainless steel on carbon steel. J Iron Steel Res Int 2009;16:44–53. https://doi.org/10.1016/S1006-706X(09)60009-1.
[30] da Silva LJ, D'Oliveira ASCM. NiCrSiBC coatings: effect of dilution on microstructure and high temperature tribological behavior. Wear 2016;350–351:130–40. https://doi.org/10.1016/J.WEAR.2016.01.015.
[31] Kucita P, Wang SC, Li WS, Cook RB, Starink MJ. The effects of substrate dilution on the microstructure and wear resistance of PTA Cu-Al-Fe aluminium bronze coatings. Wear 2019;440–441:203102. https://doi.org/10.1016/J.WEAR.2019.203102.
[32] Li R, Li Z, Huang J, Zhu Y. Dilution effect on the formation of amorphous phase in the laser cladded Ni–Fe–B–Si–Nb coatings after laser remelting process. Appl Surf Sci 2012;258:7956–61. https://doi.org/10.1016/J.APSUSC.2012.04.144.
[33] Cai Y, Chen Y, Manladan SM, Luo Z, Gao F, Li L. Influence of dilution rate on the microstructure and properties of FeCrCoNi high-entropy alloy coating. Mater Des 2018;142:124–37. https://doi.org/10.1016/J.MATDES.2018.01.007.
[34] Banovic SW, Dupont JN, Marder AR. Dilution and microsegregation in dissimilar metal welds between super austenitic stainless steel and nickel base alloys. Sci Technol Weld Join 2002;7:374–83. https://doi.org/10.1179/136217102225006804.
[35] Gheno T, Monceau D, Young DJ. Mechanism of breakaway oxidation of Fe–Cr and Fe–Cr–Ni alloys in dry and wet carbon dioxide. Corrosion Sci 2012;64:222–33. https://doi.org/10.1016/J.CORSCI.2012.07.024.
[36] Jonsson T, Pujilaksono B, Heidari H, Liu F, Svensson JE, Halvarsson M, et al. Oxidation of Fe–10Cr in O2 and in O2 + H2O environment at 600 °C: a microstructural investigation. Corrosion Sci 2013;75:326–36. https://doi.org/10.1016/J.CORSCI.2013.06.016.
[37] Baek JH, Jeong YH. Breakaway phenomenon of Zr-based alloys during a high-temperature oxidation. J Nucl Mater 2008;372:152–9. https://doi.org/10.1016/j.jnucmat.2007.02.011.
[38] Busso EP, Evans HE, Qian ZQ, Taylor MP. Effects of breakaway oxidation on local stresses in thermal barrier coatings. Acta Mater 2010;58:1242–51. https://doi.org/10.1016/j.actamat.2009.10.028.
[39] Karlsson S, Pettersson J, Johansson L-G, Svensson J-E. Alkali induced high temperature corrosion of stainless steel: the influence of NaCl, KCl and CaCl2. Oxid Metals 2012;78:83–102. https://doi.org/10.1007/s11085-012-9293-7.
[40] Pettersson J, Folkeson N, Johansson LG, Svensson JE. The effects of KCl, K 2SO 4 and K 2CO 3 on the high temperature corrosion of a 304-type austenitic stainless steel. Oxid Metals 2011;76:93–109. https://doi.org/10.1007/s11085-011-9240-z.
[41] Zahs A, Spiegel M, Grabke HJ. Chloridation and oxidation of iron, chromium, nickel and their alloys in chloridizing and oxidizing atmospheres at 400-700°C. Corrosion Sci 2000;42:1093–122. https://doi.org/10.1016/S0010-938X(99)00142-0.
[42] Yue X, Ren Y, Huang L, Zou S, Zhang L, Hua Y. The role of Cl- in the formation of the corrosion products and localised corrosion of 15Cr martensite stainless steel under an CO2-containing extreme oilfield condition. Corrosion Sci 2022;194:109935. https://doi.org/10.1016/J.CORSCI.2021.109935.
[43] Grabke HJ, Reese E, Spiegel M. The effects of chlorides, hydrogen chloride, and sulfur dioxide in the oxidation of steels below deposits. Corrosion Sci 1995;37:1023–43. https://doi.org/10.1016/0010-938X(95)00011-8.
[44] Eklund J, Persdotter A, Hanif I, Bigdeli S, Jonsson T. Secondary corrosion protection of FeCr(Al) model alloys at 600 °C – the influence of Cr and Al after breakaway corrosion. Corrosion Sci 2021;189:109584. https://doi.org/10.1016/j.corsci.2021.109584.
[45] Töpfer J, Aggarwal S, Dieckmann R. Point defects and cation tracer diffusion in (CrxFe1 - x)3 - δO4 spinels. Solid State Ionics 1995;81:251–66. https://doi.org/10.1016/0167-2738(95)00190-H.
[46] Van Orman JA, Crispin KL. Diffusion in oxides. Rev Mineral Geochem 2010;72:757–825. https://doi.org/10.2138/rmg.2010.72.17.
[47] Pujilaksono B, Jonsson T, Heidari H, Halvarsson M, Svensson J-E, Johansson L-G. Oxidation of binary FeCr alloys (Fe–2.25Cr, Fe–10Cr, Fe–18Cr and Fe–25Cr) in O2 and in O2 + H2O environment at 600 °C. Oxid Metals 2011;75:183–207. https://doi.org/10.1007/s11085-010-9229-z.
[48] Eklund J, Persdotter A, Ssenteza V, Jonsson T. The long-term corrosion behavior of FeCrAl(Si) alloys after breakaway

oxidation at 600 °C. Corrosion Sci 2023;217:111155. https://doi.org/10.1016/j.corsci.2023.111155.
[49] Bragg WHXXX. The structure of the spinel group of crystals. London, Edinburgh Dublin Phil Mag J Sci 1915;30:305–15. https://doi.org/10.1080/14786440808635400.
[50] Col A, Parry V, Pascal C. Oxidation of a Fe–18Cr–8Ni austenitic stainless steel at 850 °C in O2: microstructure evolution during breakaway oxidation. Corrosion Sci 2017;114:17–27. https://doi.org/10.1016/J.CORSCI.2016.10.029.
[51] Sand T, Bigdeli S, Sattari M, Andersson J, Hättestrand M, Helander T, et al. Efficacy of an external chromia layer in reducing nitridation of high temperature alloys. Corrosion Sci 2022;197:110050. https://doi.org/10.1016/J.CORSCI.2021.110050.
[52] Young DJ, Nguyen TD, Felfer P, Zhang J, Cairney JM. Penetration of protective chromia scales by carbon. Scripta Mater 2014;77:29–32. https://doi.org/10.1016/J.SCRIPTAMAT.2014.01.009.